Climate Dynamics
https://doi.org/10.1007/s00382-019-04972-1

On the seasonal variability of the Oyashio extension fronts

Baolan Wu[1] · **Xiaopei Lin**[1] · **Bo Qiu**[2]

Received: 12 April 2019 / Accepted: 29 August 2019

Abstract
Previous study reported that the annual-mean eastern Oyashio Extension (OE) front shifts northward while the western OE front has no obvious poleward shift during 1982–2017 by Wu et al. (Geophys Res Lett 45:9042–9048, 2018). Here we revisit this topic and focus on the seasonal variability and shifts of the OE fronts from 1982 to 2018, with observational reanalysis data and a 1.5-layer reduced-gravity model simulation. In winter, both the western and eastern OE fronts demonstrate consistent northward movement. While in summer, the eastern OE front still moves northward but the western OE front has no obvious and even southward shift. It is shown that the trade wind's expansion during 1982–2018 favours the northward shift of the OE fronts for both winter and summer. However, there is a local cold Ekman heat transport anomaly along the western OE front in summer, which surpasses the effect of trade wind expansion and prohibits northward movement of the front. This cold Ekman advection is due to a westerly wind anomaly induced firstly by the Atlantic Multi-decadal Oscillation (AMO) and secondly by the Pacific Decadal Oscillation (PDO). In winter, the local Ekman heat transport is less effective than in summer in changing the OE front position because of the deep mixed layer. Our study demonstrates the seasonality of the OE front shift and highlights the importance of local Ekman heat transport associated with the AMO. Our results also partly explain the rainfall changes in both winter and summer in the western Pacific Ocean in the past 37 years, since the rainband east of Japan is affected by the sea surface temperature and its front.

1 Introduction

The Oyashio Extension (OE) front is located around 40°N between the subtropical and subpolar gyres and features strong temperature and salinity gradients (Yuan and Talley 1996; Isoguchi et al. 2006). Rather than a single and continuous front, the OE front is composed of two independent systems: the western OE front between 145°E and 153°E and the eastern OE front between 153°E and 173°E exist along the latitude band of 38–43°N (Qiu et al. 2017). Over the past 36 years from 1982 to 2017, the annual-mean eastern OE front shifted northward while the annual-mean western OE front exhibited no obvious shift (Wu et al. 2018). Wu et al. (2018) argued that the different shift pattern between the two OE fronts was due to the large-scale wind forcing and local Ekman heat transport. While our previous study has identified the differences between the western and eastern OE fronts in their annual-mean conditions, it remains unclear if any seasonality exists in the shift of the OE fronts. In fact, a distinct seasonal difference is observed in the OE front: the meridional gradient of sea surface temperature (SST) is more intensified in winter than in summer (Fig. 1). The shift pattern of the two OE fronts may vary in different seasons. Furthermore, the surface wind change in the North Pacific Ocean, which depends on the Aleutian Low and Subtropical High pressure systems, is the key process that controls the meridional shift of the OE fronts and can be related to dominant climate modes. The first candidate is the Pacific Decadal Oscillation (PDO, Mantua et al. 1997), which can contribute to the major decadal variability in the surface wind and sea surface temperature (SST) in the Pacific Ocean. As noted by many previous investigators (e.g., Trenberth and Hurrell 1994; Miller et al. 1994; Deser and Blackmon 1995; Nakamura et al. 1997; Qiu 2003; Taguchi et al. 2007;

Electronic supplementary material The online version of this article (https://doi.org/10.1007/s00382-019-04972-1) contains supplementary material, which is available to authorized users.

✉ Xiaopei Lin
linxiaop@ouc.edu.cn

[1] Physical Oceanography Laboratory/Institute for Advanced Ocean Study, Ocean University of China and Qingdao National Laboratory for Marine Science and Technology, Qingdao 266100, China

[2] Department of Oceanography, University of Hawaii at Manoa, Honolulu, HI, USA

Published online: 04 September 2019

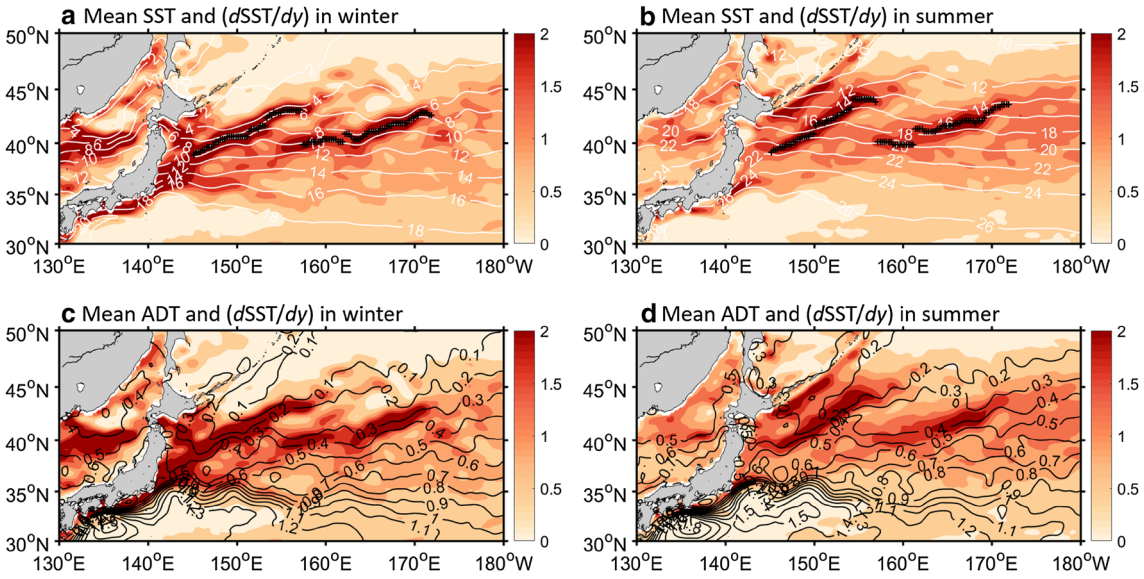

Fig. 1 **a** Mean SST (white contours, unit in degree) and meridional SST gradient (color, unit in degree per latitude) in winter during 1982–2018 derived from OISST data set. Black crosses display the mean position of the western (145–157°E) and eastern (157–172°E) OE front in winter. **b** Same as (**a**), except for the summer time. **c** Black contours indicate mean ADT (unit in m) in winter during 1982–2018 from AVISO. Color shading indicate mean meridional SST gradient (unit in degree per latitude) in winter during 1982–2018 derived from OISST data set. **d** Same as (**c**), except for the summer time. *SST* sea surface temperature, *OE* Oyashio extension, *ADT* absolute dynamic topography

Oka et al. 2012), the PDO-related decadal modulations of the Aleutian Low pressure system dominate the temporal variability of the wind stress curl anomalies near 40°N over the eastern North Pacific. A positive (negative) PDO index indicates a stronger (weaker) Aleutian low, stronger (weaker) westerlies, and lower (higher) sea surface temperature except near the North American coast. Furthermore, the wind variations induced by PDO are generated in the east central North Pacific, and the wind-induced oceanic anomalies (e.g., sea surface height, SSH) would then propagate westward at the speed of first-mode baroclinic Rossby waves. It takes 3–5 years for the anomalies reaching the western midlatitude North Pacific along ~ 40°N (Qiu et al. 2017).

Another candidate is from the Atlantic Ocean, the Atlantic Multi-decadal Oscillation (AMO). Pioneered work by Zhang and Delworth (2007) and Wu et al. (2008) proposed that the influence of the AMO on the North Pacific Aleutian Low variation (fig. 3 in Zhang and Delworth 2007; fig. 13 in Wu et al. 2008) is through atmospheric teleconnections. The AMO wind-generated variability in the central North Pacific can propagate in two ways. First, the wind-induced anomalies can propagate westward at the speed of first-mode baroclinic Rossby waves, reaching the area east of Japan after 3–5 years (Zhang and Delworth 2007), similar to the PDO-forced anomalies described in Qiu (2003). Second, the SST anomalies induced by the wind can propagate southwestward through coupled wind-evaporation-SST (WES) feedback (Xie and Philander 1994), reaching the western equatorial Pacific (Wu et al. 2008). Recently, Sun et al. (2017) proposed that the AMO-induced SST anomalies in the western equatorial Pacific can amplify through SST-sea level pressure-cloud-longwave radiation positive feedback, inducing a cyclonic (anti-cyclonic) wind anomaly in the tropical to subtropical Pacific Ocean when the SST anomalies are warm (cold). So, the AMO is another driver for the North Pacific decadal to multidecadal variability (Li et al. 2013).

Based on the aforementioned local- and inter-basin forcing mechanisms, can the wind changes in the past 37 years relating to the PDO and the AMO contribute to the seasonality and shifts of the OE fronts? To answer this question, we examine in this study the seasonal meridional shift of the OE fronts in winter and summer during the past 37 years from 1982 to 2018 by using the observational and reanalysis data. Out results show that in winter, both the western and eastern OE fronts move northward. While in summer, only the eastern OE front shows a poleward movement and the western OE front has no northward shift or even slightly moves southward. The seasonality of the OE fronts, especially why the poleward movement between the western and eastern OE fronts is different in summer, is the main focus of our present study. The paper has four sections. Section 2 shows the data and methods used in this study. In Sect. 3, we discuss the seasonal meridional shift of the OE fronts during 1982–2018. Section 3 also analyzes the dynamical and thermodynamical mechanisms and the potential effects

from the PDO and AMO. Discussion and conclusion are drawn in Sect. 4.

2 Data and methods

2.1 Data for the OE front definition

Three data sets are used in this study to characterize the seasonal shift of the OE fronts during 1982–2018: SST data, the absolute dynamic topography (ADT) data and the layer thickness anomaly (LTA, see Sect. 2.2 for more details) data from a 1.5-layer reduced-gravity model output. Basing on these three data sets, two independent OE fronts (the western OE front of 145°E–157°E and the eastern OE front of 157°E–172°E) in the North Pacific Ocean (32°N–50°N, 145°E–172°E) are defined by three methods including the maximum SST gradient, the constant value of ADT, and the constant value of LTA.

The SST data is from the National Oceanic and Atmospheric Administration (NOAA) Optimum Interpolation SST (OISST) version 2 (Reynolds et al. 2007). The SST data has a 0.25° grid in the global ocean and is daily from 1982 to 2018 (available at ftp://eclipse.ncdc.noaa.gov/). We use the maximum meridional SST gradient to identify the OE front position for both winter and summer as shown in Fig. 1 (black dots in Fig. 1a, b). The SSALTO/DUACS (2013) delayed-time multi-mission maps of the ADT is used in this study, with a monthly data of 0.25°×0.25° spatial resolution from 1993 to 2018 (available at http://www.aviso.oceanobs.com). The original altimetry data were recorded by pairs of satellites with the same ground tracks (TOPEX/POSEIDON and ERS, Jason-1 and Envisat, or Jason-2 and Envisat). Sampling by the satellites was stable over the period of our analysis. Following Qiu et al. (2017) and Wu et al. (2018), the OE front position in winter is defined by the ADT values equal to 0.2 m and 0.3 m for the western and eastern OE fronts, respectively (Fig. 1c). In summer, the ADT values equal to 0.3 m and 0.4 m are used to represent the western and eastern OE fronts as shown in Fig. 1d. The other choices of ADT values which are near the maximum meridional SST gradient in the front regions are also examined and the results are similar (figures not shown here). To exclude the global warming effect, the ADT values used in this study are detrended with a value of 1.9 mm/year for both winter and summer (Chen et al. 2017). For the LTA method, we conduct a 1.5-layer reduced-gravity model run (details in Sect. 2.2, source data can be accessed from Ocean and Atmosphere Data Center of Ocean University of China, coadc.ouc.edu.cn) and use the modelled LTA data from 1982 to 2018 to calculate the poleward movement of the OE fronts induced by surface wind forcing. Here the LTA equals to −0.7 hm is used to represent the OE fronts in both winter and summer (Fig. 2a). This is consistent with the observation (Fig. 2b) that the OE fronts are located in the southern edge of the subpolar gyre. Due to the overshooting of the Kuroshio in our 1.5-layer model, there is a systematic bias of poleward displacement of the OE fronts about 4.5°: ~45.5°N in the model (green line in Fig. 2a) and ~41°N in the observation (green lines in Fig. 2b). But the overall ocean circulation pattern of the 1.5-layer model is similar to the observations (Fig. 2).

In this study, winter (summer) climatology is defined as the mean for January to March (July to September) between 1982 and 2018. We calculate the mean position of the OE fronts in winter (summer) by using the local maximum winter (summer) climatology SST meridional gradient. In winter, the zonal mean position of the western and eastern OE fronts are around 41.23°N and 41.14°N, respectively (Fig. 1a). For summer, the zonal mean position of the western and eastern OE fronts are about 41.78°N and 41.52°N, respectively (Fig. 1b). Winter (summer) anomaly is defined as the departure from its seasonal climatology. Climatological winter and summer mixed layer depths (MLD) are calculated with a threshold value of 0.125 kg/m^3 denser than at the sea surface (Monterey and Levitus 1997). The World Ocean Atlas 2013 climatology (WOA13, Locarnini 2013;

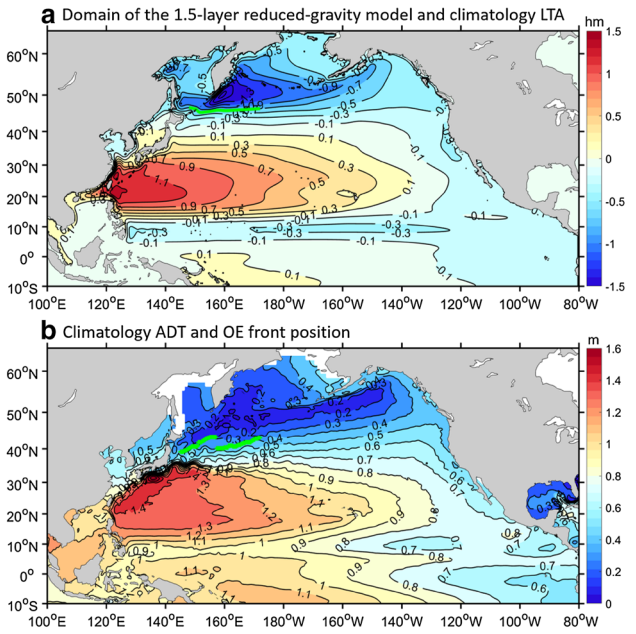

Fig. 2 **a** Domain of the 1.5-layer reduced-gravity model. The model domain covers the region from 10°S to 65°N and 100°E to 80°W with a uniform spatial resolution of 0.25°. Color and contours displays the climatological LTA (unit in hm) from model during 1982–2018. Green line indicates the −0.7 hm-contour of the LTA. **b** Color and contours displays the climatological ADT (unit in m) during 1982–2018 from AVISO. Green lines indicate the climatological position of the OE front. *LTA* layer thickness anomaly, *ADT* absolute dynamic topography

Zweng 2013) temperature and salinity data from 1975 to 2012 with a 0.25° × 0.25° spatial resolution (available at https://www.nodc.noaa.gov/OC5/woa13/woa13data.html) are used to calculate the climatological seasonal MLD. Similar to the method in Kuroda et al. (2015), we also choose the difference between two time periods, 1982–1991 and 2009–2018, to analyze the OE front decadal changes. The 95% confidence level is used in this study for all the statistical analysis, following the method of Bretherton et al. (1999).

2.2 Settings of the 1.5-layer reduced-gravity model

The governing equations for the 1.5-layer reduced-gravity model are:

$$\frac{du}{dt} - fv = -g'\frac{\partial h}{\partial x} + A\nabla^2 u + \frac{\tau^x}{\rho h}, \tag{1}$$

$$\frac{dv}{dt} - fu = -g'\frac{\partial h}{\partial y} + A\nabla^2 v + \frac{\tau^y}{\rho h}, \tag{2}$$

$$\frac{\partial h}{\partial t} + \frac{\partial (uh)}{\partial x} + \frac{\partial (vh)}{\partial y} = 0, \tag{3}$$

(e.g., Qiu and Lukas 1996), where u and v are zonal and meridional velocity, f is the Coriolis parameter, $g' = g\Delta\rho/\rho$, g is gravitational acceleration,ρ is layer density, $\Delta\rho$ is density difference between the upper and abyssal layers, A is lateral eddy viscosity coefficient, h is layer thickness, and τ^x and τ^y are zonal and meridional wind stresses, respectively.

The model domain covers the region from 10°N to 65°N and 100°E to 80°W with a spatial resolution of 0.25° (Fig. 2a). Model's bottom topography comes from the 5-min Gridded Global Relief Data (ETOPO5) bathymetry dataset interpolated onto the model grid. We use the monthly wind stress field from the ERA-I to force the model. The model is spun up first for 40 years with the mean wind stresses, and then uses the monthly wind stresses from 1979 to 2018. The lateral eddy viscosity coefficient ranges from 1.2×10^3 m^2/s to 6.8×10^3 m^2/s, with larger values used toward shallower topography. The initial layer thickness of the model is 1000 m and we define the LTA as the difference between the layer thickness and its initial value. The ρ is set to 1025 kg/m^3 and $\Delta\rho$ is 1.2 kg/m^3. This value renders the phase speed of first-mode baroclinic Rossby waves similar to that from the altimetry observations.

2.3 Wind, surface fluxes and precipitation data

Three reanalysis wind data sets are used in this study to investigate the wind changes in the past 37 years, including the NCEP/National Center for Atmospheric Research Reanalysis 1 (Kalnay et al. 1996, hereafter NCEP1), the National Centers for Environmental Predictions (NCEP)-Department of Energy Reanalysis 2 (Kanamitsu et al. 2002, hereafter NCEP2), and the European Centre for Medium-Range Weather Forecast Interim Reanalysis (Dee et al. 2011, hereafter ERA-I). The NCEP1 data we used are available from 1948 to present with 2.5° × 2.5° (latitude × longitude) spatial resolution and accessed from https://www.esrl.noaa.gov/psd/data/gridded/data.ncep.reanalysis.html. The NCEP2 data are available on a global T62 gaussian grid (192 × 94) over the 1979–2018 period and accessed from https://www.esrl.noaa.gov/psd/data/gridded/data.ncep.reanalysis2.gaussian.html. The ERA-I wind data from 1979 to present, with 0.25° × 0.25° (latitude × longitude) spatial resolution and available at http://apps.ecmwf.int/. All of the wind stress data sets have a monthly temporal resolution. To be consistent with the data period of OISST, we will analyze the wind data during the period of 1982–2018.

In addition, we use the PI-Control model experiment, which is based on the Community Earth System Model version 1.06 (Hurrell et al. 2013) of the National Center for Atmospheric Research, to further test our hypothesis of the wind changes on the OE front shift. The PI-control run starts from a standard PI-Control experiment with Community Climate System Model, Version 4 (CCSM4), which has been running for 863 years. We further run the CESM model with the same configuration for 600 years and take the last 200 years for analysis.

The surface heat flux data from NCEP1 are used in this study to investigate the effect of the local air-sea heat fluxes upon the SST anomalies in the OE front region. We use the precipitation data from the ERA-I data set to explore the rainfall changes in the Western Pacific Ocean related to the OE front shift in both winter and summer. All of above surface fluxes and precipitation data have the same temporal and spatial resolutions as the surface wind stress data.

2.4 Climate indexes

The PDO and AMO indices represent climate modes in the North Pacific and North Atlantic oceans, respectively (Mantua et al. 1997; Enfield et al. 2001). The PDO index is defined as the principal influencing factor of the monthly SST anomalies in the North Pacific Ocean, poleward of 20°N. The PDO index is available at http://www.esrl.noaa.gov/psd/data/correlation/pdo.data. The AMO index is based upon the average anomalies of SST in the North Atlantic basin, over 0°N–70°N. Data for AMO is available at https://www.esrl.noaa.gov/psd/data/timeseries/AMO/.

3 Results

3.1 Seasonal meridional shifts of the OE front

Time variability of the mean western and eastern OE front positions in winter and summer during 1982–2018 is shown in Fig. 3. It is shown that there is a clear difference of the OE front shift between winter and summer. In winter, for the period between 1982–2018, both the LTA and SST methods show consistent northward shift for the two OE fronts (see Fig. 3a, b and Table 1 for details). In the recent 27 years with the ADT observations (red line in Fig. 3a, b), both the western and eastern fronts also show consistent poleward shift trends, especially for the eastern front (see Table 1 for details). Whereas during the summer season, the eastern OE front shifts northward during 1982–2018 (Fig. 3d). However, the western OE front defined by the SST and ADT methods is relatively stable (black and red lines in Fig. 3c). The northward shift is only observed by the LTA method (blue line in Fig. 3c). It is worth noting that the OE front is foremost defined by the SST gradient rather than the sea surface height (SSH) because of its strong density compensation between the temperature and salinity variations (e.g., Yuan and Talley 1996; Jing et al. 2019). Unlike the Kuroshio

Table 1 Meridional shift trend of the western (145–157°E) and eastern (157–172°E) OE front in three methods for winter and summer time

	Western OE front	Eastern OE front
Winter time		
SST method	**0.038 ± 0.029**	**0.024 ± 0.018**
	0.049 ± 0.037	0.022 ± 0.019
ADT method	0.042 ± 0.033	0.047 ± 0.035
LTA method	**0.043 ± 0.035**	**0.046 ± 0.037**
	0.033 ± 0.027	0.023 ± 0.020
Summer time		
SST method	**−0.019 ± 0.016**	**0.034 ± 0.028**
	No obvious trend	0.029 ± 0.027
ADT method	No obvious trend	0.046 ± 0.037
LTA method	**0.034 ± 0.030**	**0.057 ± 0.040**
	0.025 ± 0.021	0.040 ± 0.033

Units are in degree per year. Values in bold and normal mean the trends of the OE front during 1982–2018 and 1993–2018, respectively. All the values are significant at the 95% confidence level. Confidence intervals are estimated through bootstrapping (one standard deviation)

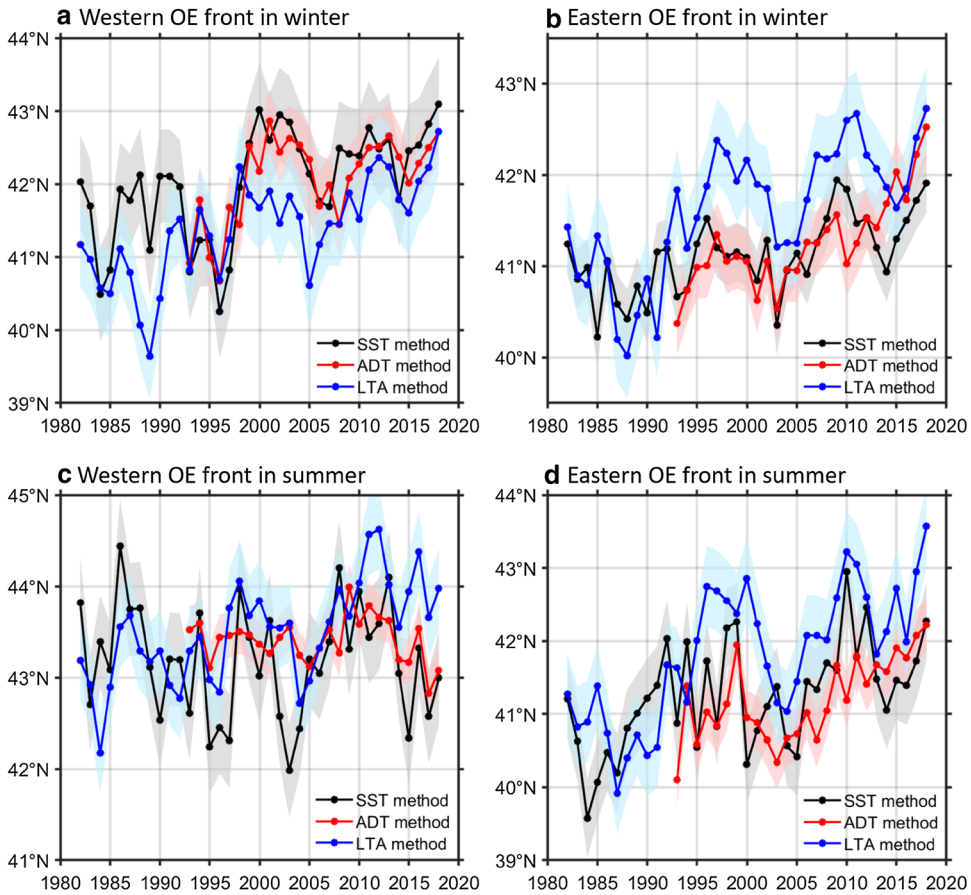

Fig. 3 **a** Variability of the zonal-averaged western OE front position from 1982 to 2018 in winter. Black, red and blue lines are the SST gradient method, ADT method (ADT = 0.2 m) and LTA method (LTA = − 0.7 hm) for the OE front definitions, respectively. The shadings of each line show the errors, calculated by the one standard deviations of the zonal-averaged OE frontal position time series. **b** Same as (**a**) but for the eastern OE front in winter time and ADT equals to 0.3 m (red line). **c**, **d** Same as (**a**, **b**), but for summer time (ADT = 0.3 m for western front, ADT = 0.4 m for eastern front). *OE* Oyashio extension, *SST* sea surface temperature, *ADT* absolute dynamic topography, *LTA* layer thickness anomaly. Details of the trend are listed in Table 1

Extension front, the ADT signal is relatively week along the OE front (e.g., Qiu et al. 2017).

According to the previous study (Wu et al. 2018), the annual mean eastern OE front has moved poleward during the past 36 years, but there is no obvious movement by the western front. In light of our results shown in Fig. 3, it indicates that the relatively steady position of the annual-mean western OE front is due to the summer, rather than winter, signals.

3.2 OE front shift by wind forcing

According to the previous studies (e.g., Wu et al. 2018), the surface wind controls the OE front shift. Figure 4a, b show the mean wind stress curl (WSC) and wind vector field in winter versus summer in the past 37 years based on the NCEP1 data set. Not surprisingly, the wind is stronger in winter than in summer. Both in winter and summer, the mean position of the OE fronts is located in the positive WSC region with westerly wind forcing, about 41°N, which is north of the zero WSC line. The seasonality of surface wind field is also reflected by the change of the mean OE front position in winter and summer as we described in Sect. 2.1. In winter, the easterly trade wind only reaches to about 25°N (Fig. 4a) and there is broad westerly wind north of this latitude. In summer, the easterly trade wind could reach to about 30°N (Fig. 4b). So, the mean OE front position in summer is closer to polar region than that in winter (Fig. 1). Figure 4c, d respectively show the surface wind and WSC decadal changes during 1982–2018 in winter and summer (decadal changes are between 1982–1991 and 2009–2018, latter minus former). In the western Pacific Ocean for both winter and summer, between 20°N to 30°N, there is a broad easterly wind anomaly, comparing with positive WSC trend, resulting in a stronger trade wind, decreasing the negative WSC in the subtropical ocean and a poleward shift of the trade wind. Overall, the trade wind strengthens and expends (Lucas et al. 2014) in both seasons, which implies a possible poleward shift of the OE fronts as suggested by our previous study (Wu et al. 2018). The above results are also confirmed by the NCEP2 and ERA-I wind data sets as shown in Supplementary Figs. S1 and S2, respectively.

As we discussed in Sect. 2.1, the OE front can be represented by the ADT or the Sverdrup streamline. Based on the hydrographic data up to 137°E along the 24°N section, Hautala et al. (1994) concluded that the Pacific subtropical gyre circulation is well explained by the Sverdrup transport (Sverdrup 1947). The Sverdrup volume transport stream function ψ is calculated from the Sverdrup relation as following:

$$\psi = -\frac{1}{\beta\rho}\int_{x_e}^{x} curl\tau dx, \tag{4}$$

where a right-handed Cartesian coordinate system is adopted with x and y axes directed in the eastward and northward directions, respectively. Here β is the y derivative of the Coriolis parameter f; the path of integration is taken zonally from the eastern boundary x_e to x, and a boundary value of 0 is assumed at the coast. To better understand the relationship among the zero WSC line, the OE front position and the zero Sverdrup streamline, we plot in Fig. 5a their climatological

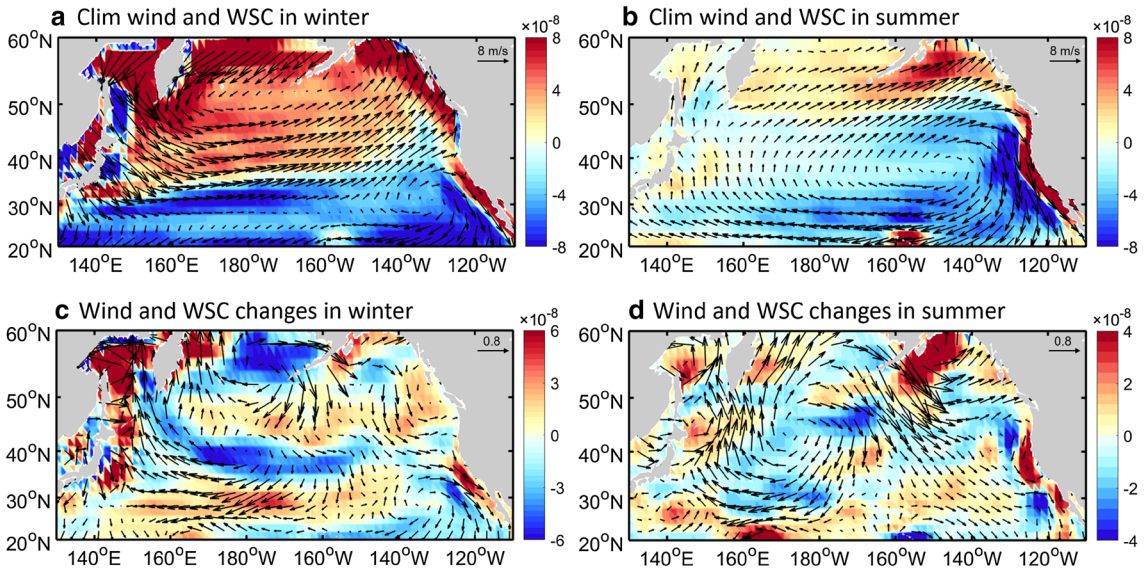

Fig. 4 **a** Climatological wind (vector, unit in m/s) and WSC (color, unit in N/m^3) in winter during the period from 1982 to 2018 derived from NCEP1 data sets. **b** Same as (**a**), but for summer time. **c** Wind (vector, unit in m/s) and WSC (color shading, unit in N/m^3) decadal changes between 1982–1991 and 2009–2018 (latter minus former) in winter. **d** As (**c**), except for summer. *WSC* wind stress curl

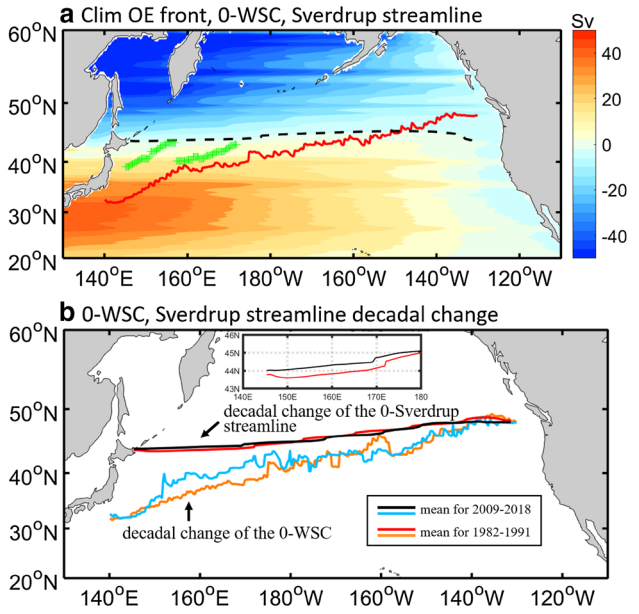

Fig. 5 **a** Schematic relationship among the climatological OE front position (green lines), zero WSC line (red line) and zero Sverdrup stream line (dashed black line) during the period from 1982 to 2018 derived from NCEP1 and OISST data sets. Color shading displays the Sverdrup volume transport streamfunction (unit in Sv, 1 Sv = 1×10^6 m^3/s) calculated from the NCEP1 wind. **b** Decadal changes of the zero WSC line and zero Sverdrup streamline between 1982–1991 and 2009–2018. The black and blue lines indicate the mean position for 2009–2018. The red and orange lines indicate the mean position for 1982–1991. *WSC* wind stress curl, *OE* Oyashio extension

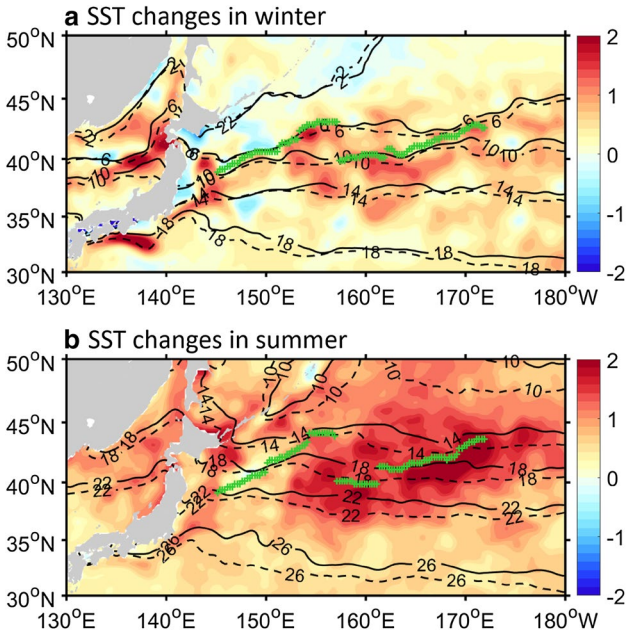

Fig. 6 **a** SST decadal changes between 1982–1991 and 2009–2018 (color shading, unit in degree) in winter during period from 1982 to 2017 based on OISST data. The black dashed and solid contours indicate the mean winter SST for 1982–1991 and 2009–2018, respectively (unit in degree). Green dots indicate the mean position of the OE front in winter. **b** As (**a**), except for summer. *SST* sea surface temperature, *OE* Oyashio extension

locations in the North Pacific. It's clear that the mean position of the OE fronts is located north of the zero WSC line and in the positive WSC area as described above (Fig. 4a, b). We should emphasize that the Sverdrup streamline, which can be considered as the SSH or LTA in the two-layer model, is an integration of WSC from the eastern coast. If the WSC is in zonal pattern (e.g., the wind field is zonal, no meridional component), the Sverdrup streamline will follow the zero WSC line. But in the real ocean, the WSC is not zonally uniformed and the zero WSC is tilted from southwest to northeast in the North Pacific Ocean. Even though the relationship will be more complicated between the zero WSC line and the zero Sverdrup streamline due to the zonally nonuniform WSC, an expansion of the wind field as represented by the displacement of the zero WSC line would induce a poleward movement of the Sverdrup streamline. It is confirmed in Fig. 5b (also see fig. 3c in Wu et al. 2018) that the zero Sverdrup streamline would move northward due to the change of WSC and resulting in poleward movement of the OE fronts in the past 37 years.

Based on the Sverdrup dynamics discussed in this section, the OE fronts should move northward no matter in winter or summer, which is confirmed by the LTA method (blue lines in Fig. 3). But the western OE front is stable and shows no poleward moving in summer, as shown in Fig. 3c with the SST method (black line in Fig. 3c). So, here comes the question: why the summer western OE front does not shift as defined by the maximum SST gradient method? We will address this question in the following section.

3.3 Thermodynamic effect on the OE front movement

We should emphasize that in the 1.5-layer reduced-gravity model, there is only wind forcing and no thermodynamics. The difference between the SST and LTA methods, therefore, implies that the thermodynamical process is also important for the OE front position variability. In fact, changes in SST by the thermodynamical process could also affect the local SST front position. For example, the front would move northward with the stronger warming in its southern part, and vice versa. As shown in Fig. 6, the different shift pattern of the two fronts in winter and summer is clearly shown in their SST decadal changes. In winter, a warming occurs in the south of the OE fronts, while no warming or even cooling in the north of the OE fronts (Fig. 6a). From the difference of SST contours between 1982–1991 (black dashed lines) and 2009–2018 (black solid lines) in Fig. 6a, the SST contours and then the SST fronts in winter move northward

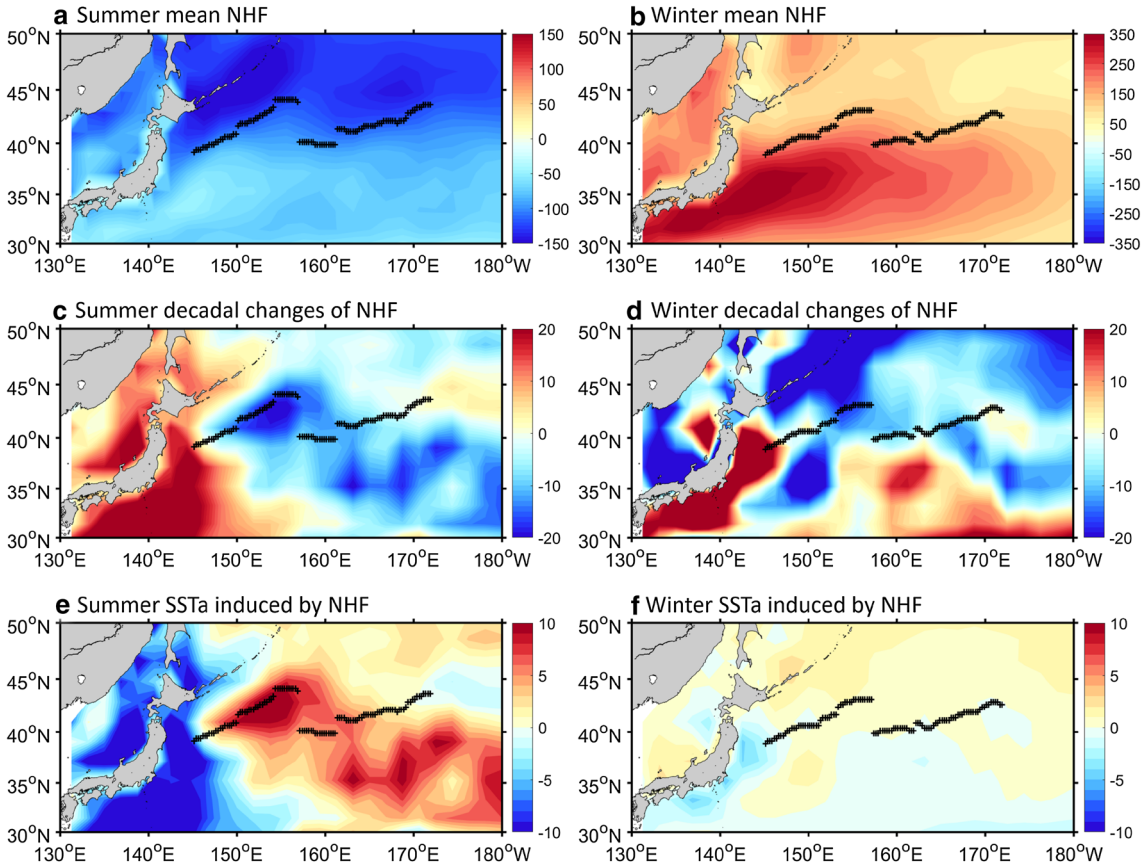

Fig. 7 **a** Climatological NHF (unit in W/m^2) in summer during 1982–2018 from the NCEP1 data. **b** As (**a**) but for winter. **c** Decadal changes of the summer NHF between 1982–1991 and 2009–2018 (latter minus former, unit in W/m^2). **d** As (**c**) but for winter. **e** SST anomalies caused by NHF (unit in degree). Black dots display the mean OE front position in summer during 1982–2018. **f** As (**e**) but for winter. *SSTa* sea surface temperature anomalies, *NHF* net heat flux, *OE* Oyashio extension

for the two OE fronts. In summer, the same condition happens for the eastern OE front with surface temperature warming stronger in the southern part than the northern part, leading to the poleward moving of the front. However, when we look at the western OE front, SST warming is broad and week in both northern and southern areas of the front, making it relatively stable (Fig. 6b). The patterns of SST decadal changes are consistent with the OE front shift shown in Fig. 3 and Table 1, especially for the different shift patterns between the western and eastern parts in summer. Up to now, it's clear that both the wind field changes and local SST changes favour the winter poleward movement of the OE fronts. But for summer, local SST changes, rather than the basin scale wind changes, control the western OE front variability. Next, we try to analyze the mechanism responsible for the different OE front shift between the western and eastern parts in summer.

Following Wu et al. (2018), we consider the ocean heat budget in the mixed layer, which affects the SST and then the OE front position. Due to the limitation in observations, we cannot calculate all terms in the heat budget equation. Here we focus on the two major terms in the right-hand side of the SST governing Eq. (5), heat flux and advection, as shown in the following:

$$\frac{\partial SST}{\partial t} = \frac{Q_{net}}{C_p \rho H_m} - v \cdot \nabla SST + R, \tag{5}$$

where Q_{net} is the net heat flux (NHF), C_p is the specific heat of seawater, ρ is the seawater density and H_m is MLD (see Sect. 2). In this study, the H_m is only used with the climatological summer (or winter) value. The term $\frac{Q_{net}}{C_p \rho H_m}$ and $v \cdot \nabla SST$ represent the thermal effect of NHF and advection to the SST change, respectively. R is the residual term and will be ignore in this study (Qiu and Kelly 1993). For the advection term:

$$v \cdot \nabla SST = U_E \cdot \frac{\partial SST}{\partial x} + V_E \cdot \frac{\partial SST}{\partial y} = \frac{\tau_y}{f H_m \rho} \cdot \frac{\partial SST}{\partial x} - \frac{\tau_x}{f H_m \rho} \cdot \frac{\partial SST}{\partial y}, \tag{6}$$

where f is the Coriolis parameter and τ_y and τ_x are the surface wind stress in the y and x directions, respectively. The previous study by Larson et al. (2018) confirmed that the

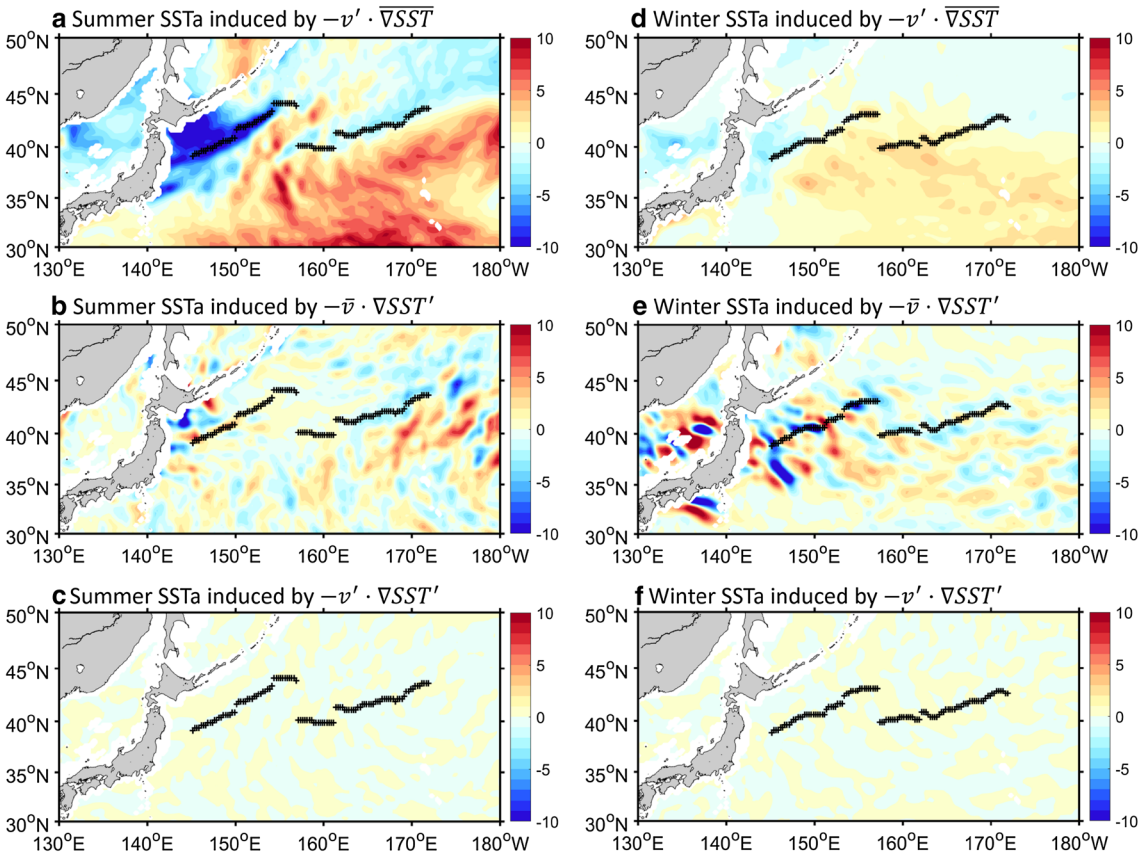

Fig. 8 **a** SST anomalies caused by Ekman heat transport term $-v' \cdot \overline{\nabla SST}$ (color shading, unit in degree) and the mean OE front position (black dots) in summer during 1982-2018 based on the NCEP2 data sets. **b**, **c** As (**a**) but for $-\bar{v} \cdot \nabla SST'$ and $-\bar{v} \cdot \nabla SST'$, respectively. **d–f** As (**a–c**), but for the winter time. *SSTa* sea surface temperature anomalies, *OE* Oyashio extension

Ekman heat transport is dominant in the OE front region. Based on their research, we only analyzed the advection term by evaluating the three Ekman terms, $-v' \cdot \overline{\nabla SST}$, $-\bar{v} \cdot \nabla SST'$ and $v' \cdot \nabla SST'$, where overbars denote the climatological mean value and primes, the deviation from the mean.

Figure 7 displays the contribution of the NHF to the SST anomalies for both seasons. From the mean NHF field (Fig. 7a, b), the ocean absorbs heat from the atmosphere (vice versa for the winter) but the value is much less than winter, which is common because the winter air-sea interaction is much stronger than summer. When we look at the decadal changes of NHF field (Fig. 7b, c), the summer value is basically equal to winter's. Finally, we find that the SST anomaly induced by NHF decadal changes is more obvious in summer than in winter (Fig. 7e, f). But we should emphasize that the warmer SST appears in the southern OE front region for both western and eastern parts (Fig. 7e), which favours the poleward shift of the whole OE front. This cannot explain the observed west–east pattern of the summer SST anomalies as shown in Fig. 6b. For the advection term, the anomalous Ekman velocity ($-v' \cdot \overline{\nabla SST}$ term) is dominant and more important than the other two terms ($-\bar{v} \cdot \nabla SST'$ and $v' \cdot \nabla SST'$) for the SST changes in both summer and winter as shown in Fig. 8. In summer, it shows cooling effect in the northwest Pacific Ocean and warming effect in the southeast Pacific Ocean. The heat transport by mean Ekman velocity ($-\bar{v} \cdot \nabla SST'$ term, Fig. 8b) is patchy and also smaller than the anomalous Ekman velocity term (Fig. 8a). The advection by the two anomalous term ($v' \cdot \nabla SST'$) is very small and can be neglected (Fig. 8c). The above features also works in winter as shown in Fig. 8d–f. In fact, we found that the warm Ekman heat transport in the eastern OE front region (red shadings in Fig. 8a) and the cold Ekman heat transport in the western OE front region (blue shadings in Fig. 8a) by the anomalous Ekman velocities determine the west–east dipole pattern of summer SST anomalies in the past 37 years as discussed in Fig. 6b. This west–east dipole pattern is also consistent with the OE front shift in summer (Fig. 3c, d). As for the summer eastern OE front (157°E–172°E), the SST increases due to the warm Ekman heat transport, shifting the front northward (Figs. 3d, 6b, 8a and Table 1). On the contrary, for the western OE front part (145°E–157°E) in summer, the SST decreases by

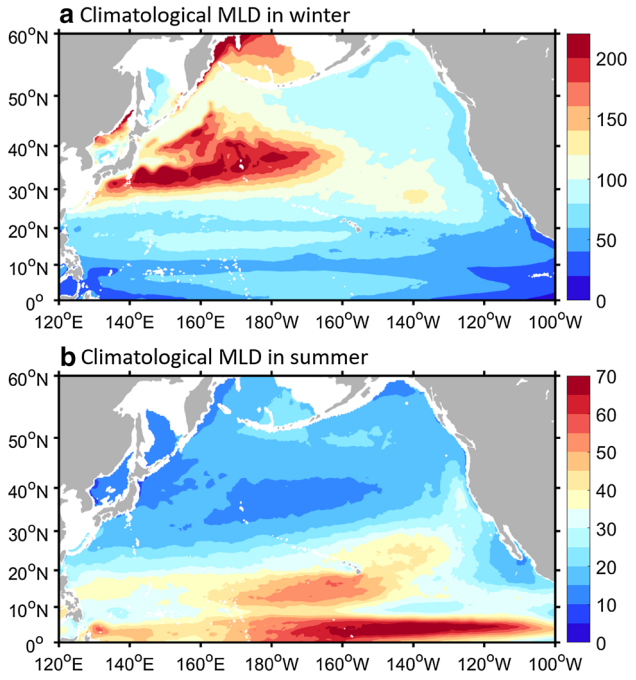

Fig. 9 **a** Climatological MLD in winter (unit in m) during 1975–2012 from WOA13 data sets. **b** As (**a**), except for summer. *MLD* mixed layer depth

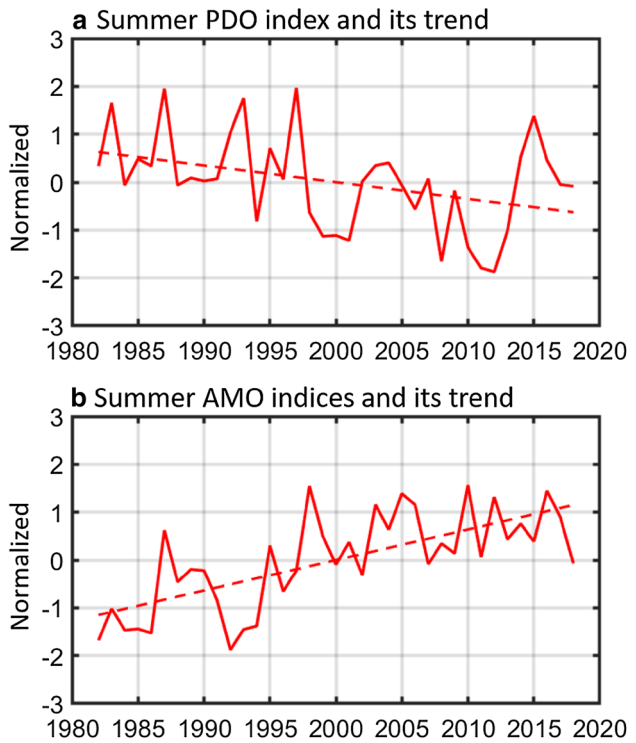

Fig. 10 **a** Time series of the normalized PDO index (solid line) and its trend (dashed line) in summer from 1982 to 2018. **b** Same as (**a**), except for the normalized AMO index. Both the trends of PDO and AMO indices are significant at the 95% confidence level. *PDO* Pacific decadal oscillation, *AMO* Atlantic multi-decadal oscillation

the cold Ekman heat transport, resulting in no poleward or even southward shift of the front as indicated by Fig. 8a (also see Figs. 3c, 6b and Table 1). It is demonstrated that the west–east different pattern of the OE front shift in summer is caused by the different local Ekman heat transport induced by the anomalous Ekman velocities. The above results of the SST anomaly induced by Ekman heat transport are also confirmed by the NCEP2 and ERA-I wind data sets as shown in Supplementary Figures S3 and S4, respectively. What's more, we notice that the local SST changes in summer is much more important than in winter, which means the summer SST anomalies is more sensitive to the variability of either the NHF or the wind than in winter time (Figs. 7 and 8). Figure 9 compares the mean MLD distributions in winter and summer. It is clear that the summer MLD is much shallower than that in winter: the winter MLD in the OE front region is usually larger than 100 m or even reaches 200 m (Fig. 9a), but only around 20 m (Fig. 9b) in summer. The SST anomaly caused by both NHF and wind-induced Ekman advection are proportional to the inverse of MLD, as shown in Eqs. (5) and (6). It is concluded that the mean atmospheric forcings (NHF and wind) in summer are weaker than in winter, but their changes are in similar values in both seasons in the past 37 years. As a result, the local SST changes around the OE front region are larger in summer than in winter due to the seasonality of the MLD.

As discussed above, the local anomalous Ekman velocity caused by wind changes is the key process that controls the summer OE front movement. Tracing back to Fig. 4d (also see Supplementary Figs. S1d and S2d) in the past 37 years, the wind anomaly is westward in the mid-latitude in the North Pacific Ocean, which will induce warm Ekman heat transport and then push the eastern OE front moving poleward. In the western OE front, the wind anomaly switches to westerly wind and induces cold Ekman heat transport, shifting the front southward. In the next section, we will further explore the relationship between the wind changes and the climate modes, PDO and AMO, for the summer time.

3.4 Potential impact from PDO and AMO

During the past 37 years from 1982 to 2018, the summer PDO and AMO indexes are in the same pace after late 1970s: summer PDO (AMO) index decreases (increases) as shown in Fig. 10. How are the decrease (increase) of the PDO (AMO) related to the wind changes and then the meridional shift of the OE fronts? We first examine the relationship between the wind changes and PDO in the North Pacific, and also the AMO according to previous studies (e.g. Sun et al. 2017). Figure 11 demonstrates the wind vector regressed upon the normalized PDO and AMO during 1982–2018 with three wind data sets (NCEP1, NCEP2 and ERA-I), respectively. In summer, both the PDO- and

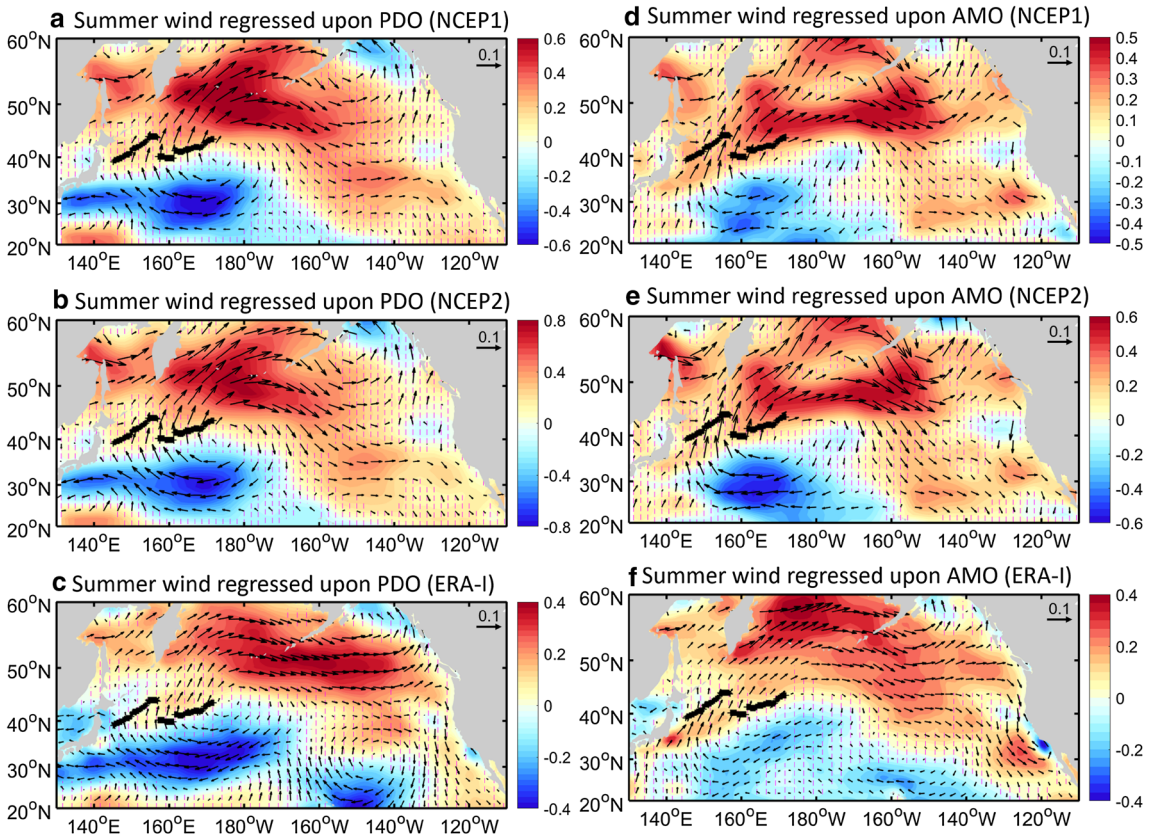

Fig. 11 **a** Wind vectors regressed upon the normalized PDO index for summer during 1982–2018 with NCEP1 data sets. Color shading indicates the u component of the wind (unit in m/s). Magenta lines indicate the regression coefficients statistically significant below the 5% significance level. Black dots indicate the mean position of the OE front in summer. **b**, **c** Same as (**a**) but based on the NCEP2 and ERA-I data sets, respectively. **d** As (**a**) but regressed upon the normalized AMO index. **e**, **f** Same as (**d**) but based on the NCEP2 and ERA-I data sets, respectively. *PDO* Pacific decadal oscillation, *AMO* Atlantic multi-decadal oscillation, *OE* Oyashio extension

AMO-induced wind changes show apparent easterly wind anomalies (blue shading in Fig. 11) in the subtropical North Pacific. Specifically, the wind pattern associated with the PDO, evaluated by regressing the grid-point wind vectors onto the normalized PDO, demonstrates easterly wind anomalies over the whole southern area of the eastern OE front and westerly wind anomalies over the whole northern area of the western OE front (Fig. 11a–c). These wind changes favour a northward warm Ekman heat transport in the eastern OE front region and a southward cold Ekman heat transport in the western OE front region, making the eastern OE front moving poleward and the western OE front equatorward. Consistently, the wind changes induced by the AMO is also different in the western and eastern OE fronts, similar to the PDO (Fig. 11d–f). Both the PDO and AMO induce the similar dipole pattern of Ekman heat transport as discussed in Sect. 3.3. The effects on the SST and then the OE front shift by the PDO- and AMO-induced wind changes can be further confirmed in Fig. 12. The SST anomalies by the PDO-induced Ekman heat transport have a broad warming pattern in the south of the eastern OE front, especially around 160°E, which will favour the northward shift of the eastern OE front as indicated by the new position of the OE front (red dots of the eastern OE front in Fig. 12a). In the western OE front region, the SST changes by the PDO-induced Ekman heat transport is cold and the western OE front in this case shifts southward (red dots of the western OE front in Fig. 12a). The SST changes by the AMO-induced Ekman heat transport has a similar dipole pattern, warm SST anomalies in the eastern OE frontal region and cold SST anomalies in the western OE front region (Fig. 12b), resulting in the southward shift of the western parts and northward shift of the eastern parts. Both the PDO- and AMO-induced Ekman heat transports are consistent with the wind vectors regressed upon the PDO and AMO indices and are also consistent with the different shift patterns of the two OE fronts. We should note here that in the past 37 years, PDO experienced a peak-trough-peak variability, making its contribution to the 37-year trend to be smaller than that of AMO, which switched from its negative to positive phase. That is the reason why the PDO-induced

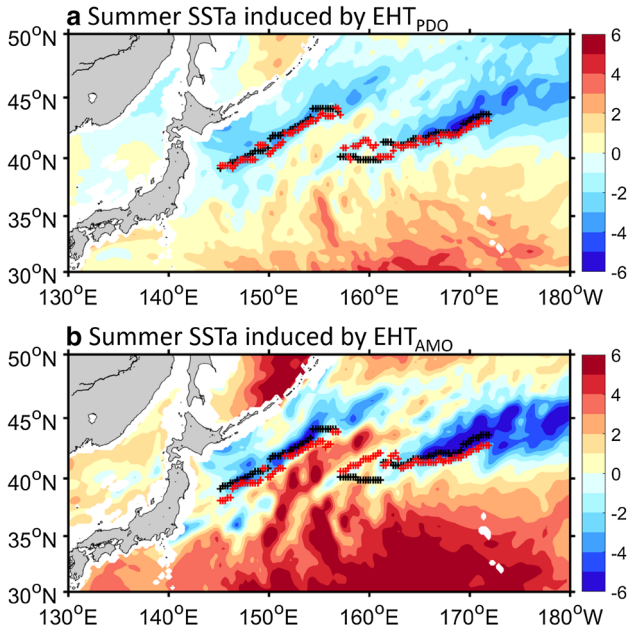

Fig. 12 **a** Summer SST anomaly caused by the EHT term $-v' \cdot \overline{\nabla SST}$ (color shading, unit in degree) of PDO during 1982–2018. The EHT term is calculated by the PDO induced wind time series, which is from the NCEP1 wind vector regressed upon the PDO index for summer season during 1982–2018. Black dots indicate the mean position of OE front and red dots indicate the new position of OE front after considering summer SST anomaly induced by EHT term of PDO during 1982–2018. **b** As (**a**) but based on the AMO index. *SSTa* sea surface temperature anomalies, *EHT* Ekman heat transport, *PDO* Pacific decadal oscillation, *AMO* Atlantic multi-decadal oscillation, *OE* Oyashio extension

SST change and OE front shift are smaller than that by the AMO over the past 37 years (Fig. 12).

Local air-sea heat flux is also important and we cannot exclude its impact on the SST and frontal changes in the OE front region. To further explore the role of local air-sea heat flux anomalies by PDO and AMO, we regress the grid-point NHFs upon the normalized PDO and AMO indices (Fig. 13) from 1982 to 2018. For both the PDO- or AMO-regressed NHF patterns, they all show similar patterns with weak heat gain from the atmosphere in the OE front region (blue shadings near the OE front region in Fig. 13a, b). From the SST changes induced by the regressed heat flux anomalies (Fig. 13c, d), both the PDO and AMO would warm the ocean and increase SST in the OE front region. As such, the local heat flux cannot explain the observed differences of the SST and front changes between the western and eastern OE fronts.

Here, we conclude that both the PDO and AMO contribute to the different movement of the western and eastern OE fronts in summer in the past 37 years, through the local Ekman heat transport. The PDO- and AMO-induced NHF forcing plays little role for this west–east different shifting pattern.

4 Discussion and conclusion

In this study, we investigated the seasonality of meridional shift of the OE fronts in the past 37 years from 1982 to 2018. In winter, both the western and eastern OE fronts move northward. In summer, the eastern OE front moves northward while the western OE front has no obvious movement. The long-term OE front variability is largely controlled by the changes in the surface wind field. In the past 37 years, the trade wind in the North Pacific Ocean expanded and strengthened, which favoured a northward shift of the two OE fronts in both seasons. Our study further highlights the importance of the local wind forcing in summer, especially for the western OE front. The Ekman heat transport by the local wind anomalies in the western OE front region decreased the SST and shifted the western OE front southward. This process worked to cancel the poleward movement of the western OE front induced by the large-scale wind or the local heat flux forcing and led to a relatively stationary state. Our results suggest that the local wind forcing via Ekman heat transport should not be ignored in the OE front region, especially in summer. It is worth emphasizing that the winter wind and its variability are usually larger than those in summer. But the Ekman heat transport is more important in summer than that in winter due to the seasonality of the MLD (Fig. 9). Since the SST change by Ekman heat transport is inversely proportional to the MLD (as shown in Eq. 6), the thin MLD in summer makes the Ekman heat transport much more dominant as compared to the winter season (Fig. 8).

One of the key processes that controls the OE front variability, as discussed above, is the local Ekman heat transport, which links the change of SST and then the OE front to the change of wind field. The expansion of the trade winds and then the enhanced warm Ekman heat transport contributes to the poleward shift of OE front in both winter and summer. Since the observation is limited, we further test the relationship among the wind, Ekman heat transport, SST and OE front position with a climate model. We use the 200-year wind stress and SST output data from the PI control model experiment as described in Sect. 2.3. Figure 14a shows the mean wind stress and WSC in the North Pacific. They are consistent with the observations (Fig. 4a) that the trade wind occupies the subtropical ocean with negative WSC and the westerly wind occupies the subpolar ocean with positive WSC. The mean position of the OE front is located along about 43°N (black dots in Fig. 14b), which is further north than the observations due to the overshooting of the climate model. We should point out that the resolution of the climate

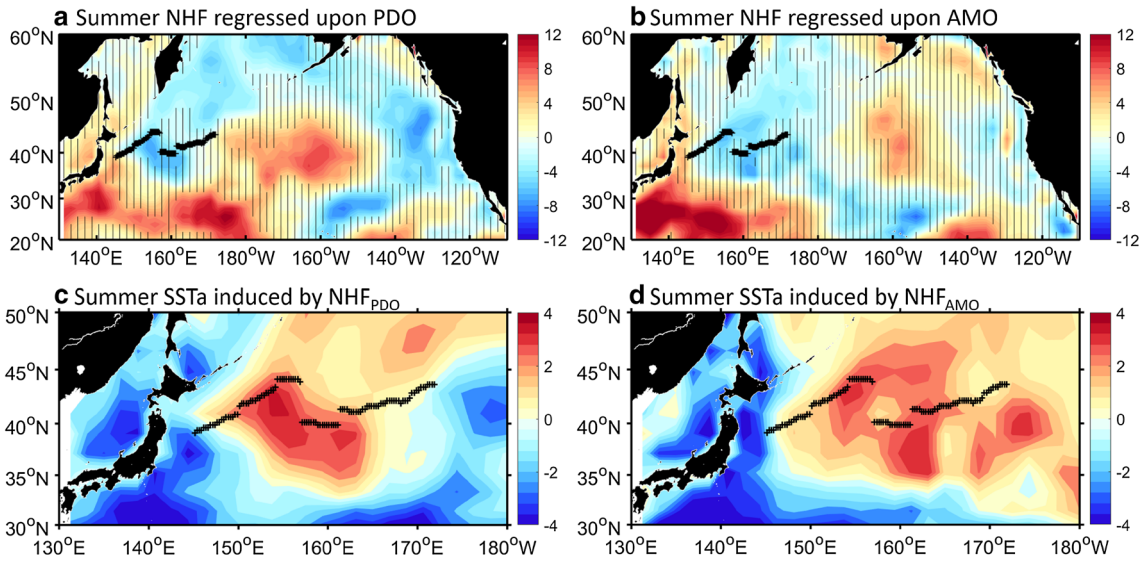

Fig. 13 **a** NHF regressed upon the normalized PDO index for summer during 1982–2018 with NCEP1 data sets (unit in W/m^3). Grey lines indicate the regression coefficients statistically significant below the 5% significance level. Positive means upward heat release from ocean to atmosphere. **b** As (**a**) but for AMO index. **c** SST anomaly induced by NHF which is regressed upon the normalized PDO index for summer during 1982–2018 with NCEP1 data sets (unit in degree). Black dots indicate the mean position of the OE front in summer. **b** As (**a**) but based on the NHF regressed upon the normalized AMO index. *NHF* net heat flux, *PDO* Pacific decadal oscillation, *AMO* Atlantic multi-decadal oscillation, *OE* Oyashio extension

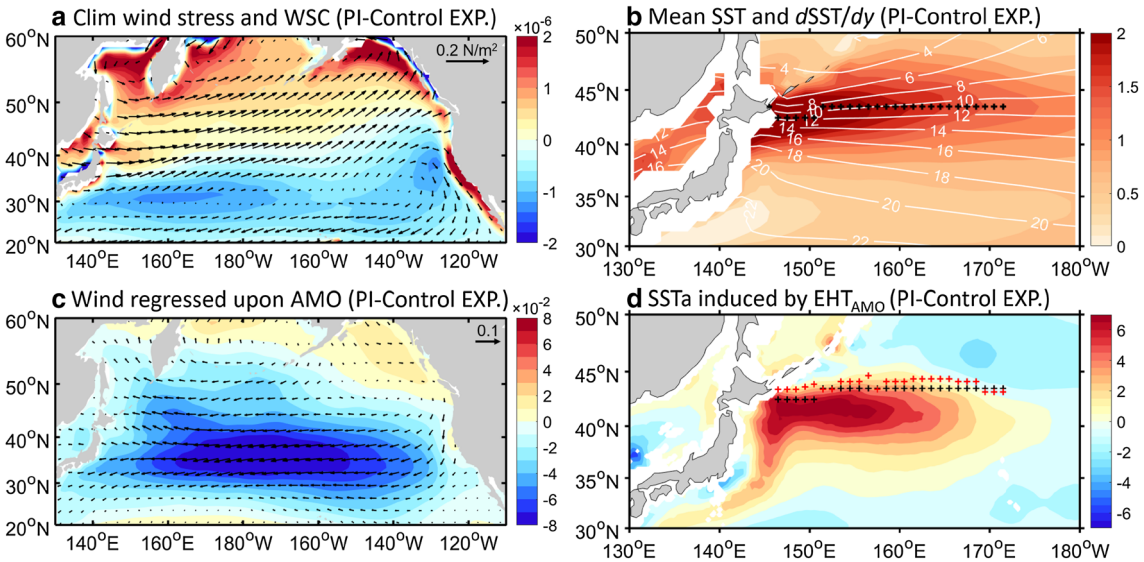

Fig. 14 **a** Climatological wind stress (vector, unit in N/m^2) and WSC (color, unit in N/m^3) from the 200-year modelling output of the PI-Control experiment. **b** Mean SST (white contours, unit in degree) and meridional SST gradient (color, unit in degree per latitude) derived from PI-Control experiment data set. Black crosses display the mean position of the OE front. **c** Wind vectors regressed upon the model AMO index from the PI-Control experiment. Color shading indicates the surface wind stress in the x direction (unit in N/m^2). **d** SST anomaly caused by the EHT term $-v' \cdot \overline{\nabla SST}$ (color shading, unit in degree) of modelled AMO. The EHT term is calculated with the wind of (**b**). Black dots indicate the mean position of OE front and red dots indicate the new position of OE front after considering summer SST anomaly induced by EHT term of AMO

model is coarse and cannot resolve the OE front very well. There are no clear western and eastern parts of the OE front in the climate model, only one continuous front as shown in Fig. 14b. In Sect. 3, we proposed that in the past 37 years, the trade wind expansion is firstly due to the phase change of AMO and secondly to PDO. Here, we check the model

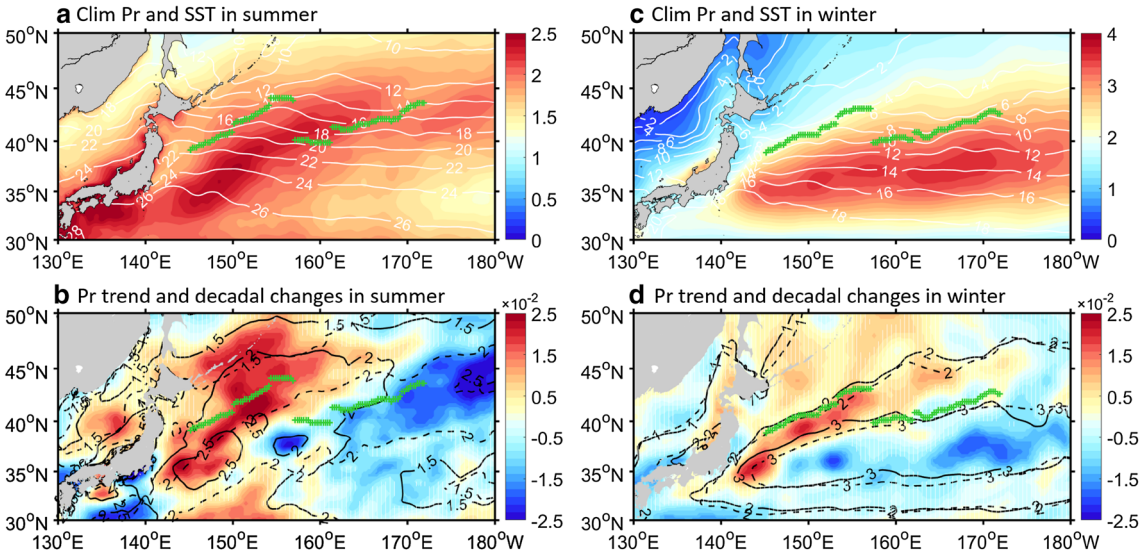

Fig. 15 **a** Climatological Pr and SST in summer during the period from 1982 to 2018 based on ERA-I data. **b** The color shading denotes Pr trend (unit in mm/year) in summer during the period from 1982 to 2018 based on ERA-I data. The black dashed and solid contours indicate the mean summer Pr for 1982–1991 and 2009–2018, respectively (unit in mm). White lines indicate the trends are blow the 5% significance level. Green dots indicate the mean position of the OE front in summer. **c**, **d** As (**a**) and (**b**), except for winter time. *Pr* precipitation, *SST* sea surface temperature, *OE* Oyashio extension

output to see whether the wind change by the modelled AMO could induce the similar expansion of trade wind, and then the warm Ekman heat transport, increased SST and poleward shift of the OE front as we show in the last section. Figure 14c is calculated by regressing the wind stress upon the modelled AMO index. It shows similar easterly wind anomalies in the broad subtropical to subpolar ocean, implying expansion of the trade wind. This wind anomaly results in warm Ekman heat transport and increased SST in the OE front region, and pushes the OE front northward (Fig. 14d). In summary, both observations and this model experiment confirm that the Ekman heat transport induced by the wind changes is the key process controlling the SST and OE front variability in the North Pacific Ocean.

The OE front has strong impact on the local atmosphere, such as anchoring the storm tracks and the rainband. Previous studies already reported the northward shift of storm tracks in the North Pacific Ocean and indicated the SST changes contribute to this shift (Wang et al. 2017). The local maximum rainfall in the North-western Pacific Ocean in both winter and summer is also along the southern rim of the OE front (Fig. 15a, b). The heating from ocean and the location of SST front may contribute to anchor the position of the rainband (Minobe et al. 2010). Figure 15c, d show the rainfall trend in winter and summer during 1982–2018. It is clear that the rainband in winter moves northward along with the OE front poleward shift (Fig. 15c, see the 2 mm/day and 3 mm/day contours' changes). In summer, the rainband change exhibits a similar dipole pattern as the OE front shift (Fig. 3c, d), with a rainband position stagnation in the western OE front and a poleward movement in the eastern OE front (Fig. 15d). The above results imply the shift of the OE fronts can also be reflected in the rainfall changes and affect the local climate.

Acknowledgements Xiaopei Lin is supported by the China's national key research and development projects (2016YFA0601803), the Qingdao National Laboratory for Marine Science and Technology (2017ASKJ01) and the National Natural Science Foundation of China (41490641, 41521091 and U1606402). The software used to generate all the results in this study is MATLAB.

References

Bretherton CS, Widmann M, Dymnidov VP, Wallace JM, Blade I (1999) The effective number of spatial degrees of freedom of a time-varying field. J Clim 12:1990–2009. https://doi.org/10.1175/1520-0442(1999)012%3c1990:TENOSD%3e2.0.CO;2

Chen X, Zhang X, Church JA, Watson CS, King MA, Monselesan D, Legresy B, Harig C (2017) The increasing rate of global mean sea-level rise during 1993–2014. Nat Clim Change 7:492–497. https://doi.org/10.1038/NCLIMATE3325

Dee DP, Uppala SM, Simmons AJ, Berrisford P, Poli P, Kobayashi S et al (2011) The ERA-Interim reanalysis: configuration and performance of the data assimilation system. Q J R Meteorol Soc 137:553–597. https://doi.org/10.1002/qj.828

Deser C, Blackmon ML (1995) On the relationship between tropical and North Pacific sea surface temperature variations. J Clim 8:1677–1680. https://doi.org/10.1175/1520-0442(1995)008%3c1677:OTRBTA%3e2.0.CO;2

Enfield DB, Mestas-Nunez AM, Trimble PJ (2001) The Atlantic multidecadal oscillation and its relation to rainfall and river flows in the continental US. Geophys Res Lett 28:2077–2080

Hautala SL, Roemmich DH, Schmitz WJ Jr (1994) Is the North Pacific in Sverdrup balance along 24°N? J Geophys Res 99:16041–16052. https://doi.org/10.1029/94JC01084

Hurrell JW et al (2013) The community earth system model: a framework for collaborative research. Bull Am Meteorol Soc 94:1339–1360. https://doi.org/10.1175/BAMS-D-12-00121.1

Isoguchi O, Kawamura H, Oka E (2006) Quasi-stationary jets transporting surface warm waters across the transition zone between the subtropical and the subarctic gyres in the North Pacific. J Geophys Res 111:c10003. https://doi.org/10.1029/2005JC003402

Jing Z, Chang P, Shan X, Wang S, Wu L, Kurian J (2019) Mesoscale SST dynamics in the Kuroshio–Oyashio extension region. J Phys Oceanogr 49:1339–1352. https://doi.org/10.1175/jpo-d-18-0159.1

Kalnay E, Kanamitsu M, Kistler R, Collins W, Deaven D, Gandin L, Iredell M, Saha S, White G, Woollen J, Zhu Y, Chelliah M, Ebisuzaki W, Higgins W, Janowiak J, Mo KC, Ropelewski C, Wang J, Leetmaa A, Reynolds R, Jenne R, Joseph D (1996) The NCEP–NCAR 40-year reanalysis project. Bull Am Meteorol Soc 77:1057–1072. https://doi.org/10.1175/1520-0477(1996)077%3C0437:TNYRP%3E2.0.CO;2

Kanamitsu M, Ebisuzaki W, Woollen J, Yang SK, Hnilo JJ, Fiorino M, Potter GL (2002) NCEP-DOE AMIP-II reanalysis (R-2). Bull Am Meteorol Soc 83:1631–1643. https://doi.org/10.1175/BAMS-83-11-1631

Kuroda H, Wagawa T, Shimizu Y, Ito S, Kakehi S, Okunishi T, Ohno S, Kusaka A (2015) Interdecadal decrease of the Oyashio transport on thecontinental slope off the southeastern coast of Hokkaido, Japan. J Geophys Res 120:2504–2522. https://doi.org/10.1002/2014JC010402

Larson SM, Vimont DJ, Clement AC, Kirtman BP (2018) How momentum coupling affects sst variance and large-scale pacific climate variability in CESM. J Clim 31:2927–2944. https://doi.org/10.1175/JCLI-D-17-0645.1

Li JP, Sun C, Jin F-F (2013) NAO implicated as a predictor of Northern Hemisphere mean temperature multidecadal variability. Geophys Res Lett 40:5497–5502. https://doi.org/10.1002/2013gl057877

Locarnini RA et al (2013) World ocean Atlas 2013, volume 1: temperature. In: Levitus S (Ed) A. Mishonov technical Ed.; NOAA Atlas NESDIS 73, 40 pp

Lucas C, Timbal B, Nguyen H (2014) The expanding tropics: a critical assessment of the observational and modeling studies. Wires Clim Change 5:89–112. https://doi.org/10.1002/wcc.251

Mantua NJ, Hare SR, Zhang Y, Wallace JM, Francis RC (1997) A Pacific interdecadal climate oscillation with impacts on salmon production. Bull Am Meteorol Soc 78:1069–1079. https://doi.org/10.1175/1520-0477(1997)078%3C1069:APICOW%3E2.0.CO;2

Miller AJ, Cayan DR, Barnett TP, Graham NE, Oberhuber JM (1994) Interdecadal variability of the Pacific Ocean: model response to observed heat flux and wind stress anomalies. Clim Dyn 9:287–302. https://doi.org/10.1007/BF00204744

Minobe S, Miyashita M, Kuwano-Yoshida A, Tokinaga H, Xie SP (2010) Atmospheric response to the gulf stream: seasonal variations. J. Climate 23:3699–3719. https://doi.org/10.1175/2010jcli3359.1

Monterey GI, Levitus S (1997) Seasonal variability of mixed layer depth for the world ocean. NOAA Atlas NESDIS 14, 96 pp

Nakamura H, Lin G, Yamagata T (1997) Decadal climate variability in the North Pacific during the recent decades. Bull Am Meteorol Soc 78:2215–2225. https://doi.org/10.1175/1520-0477(1997)078%3c2215:DCVITN%3e2.0.CO;2

Oka E, Qiu B, Kouketsu S, Uehara K, Suga T (2012) Decadal seesaw of the central and subtropical mode water formation associated with the Kuroshio extension variability. J Oceanogr 68:355–360. https://doi.org/10.1007/s10872-015-0300-x

Qiu B (2003) Kuroshio Extension variability and forcing of the Pacific decadal oscillations: responses and potential feedback. J Phys Oceanogr 33:2465–2482. https://doi.org/10.1175/2459.1

Qiu B, Kelly KA (1993) Upper ocean heat balance in the Kuroshio Extension region. J Phys Oceanogr 23:2027–2041. https://doi.org/10.1175/1520-0485(1993)023%3c2027:UOHBIT%3e2.0.CO;2

Qiu B, Lukas R (1996) Seasonal and interannual variability of the North equatorial current, the Mindanao current and the Kuroshio along the Pacific western boundary. J Geophys Res 101:12315–12330. https://doi.org/10.1029/95JC03204

Qiu B, Chen S, Schneider N (2017) Dynamical links between the decadal variability of the Oyashio and Kuroshio extensions. J Clim 30:9591–9605. https://doi.org/10.1175/JCLID-17-0397.1

Reynolds RW, Smith TM, Liu C, Chelton DB, Casey KS, Schlax MG (2007) Daily high-resolution-blended analyses for sea surface temperature. J. Climate 20:5473–5496. https://doi.org/10.1175/2007JCLI1824.1

SSALTO/DUACS (2013) SSALTO/DUACS User Handbook: (M)SLA and (M)ADT Near-real time and delayed time products

Sun C, Kucharski F, Li J, Jin FF, Kang IS, Ding RQ (2017) Western tropical Pacific multidecadal variability forced by the Atlantic multidecadal oscillation. Nat. Commun 8:15998. https://doi.org/10.1038/ncomms15998

Sverdrup HU (1947) Wind-driven currents in a baroclinic ocean with application to the equatiorial currents of the eastern Pacific. Proc Natl Acad Sci USA 33:318–326

Taguchi B, Xie SP, Schneider N, Nonaka M, Sasaki H, Sasai Y (2007) Decadal variability of the Kuroshio extension. Observations and an eddy-resolving model hindcast. J Clim 20:2357–2377. https://doi.org/10.1175/JCLI4142.1

Trenberth KE, Hurrell JW (1994) Decadal atmosphere-ocean variations in the Pacifc. Clim Dyn 9:303–319. https://doi.org/10.1007/BF00204745

Wang J, Kim HM, Chang EKM (2017) Changes in Northern hemisphere winter storm tracks under the background of arctic amplification. J Clim 30:3705–3724. https://doi.org/10.1175/JCLI-D-16-0650.1

Wu L, Li C, Yang C, Xie SP (2008) Global teleconnections in response to a shutdown of the Atlantic meridional overturning circulation. J Clim 21:3002–3019. https://doi.org/10.1175/2007JCLI1858.1

Wu B, Lin X, Qiu B (2018) Meridional shift of the Oyashio extension front in the past 36 years. Geophys Res Lett 45:9042–9048. https://doi.org/10.1029/2018GL078433

Xie SP, Philander SGH (1994) A coupled ocean-atmosphere model of relevance to the ITCZ in the eastern Pacific. Tellus 46:340–350. https://doi.org/10.1034/j.1600-0870.1994.t01-1-00001.x

Yuan XJ, Talley LD (1996) The subarctic frontal zone in the North Pacific: characteristics of frontal structure from climatological data and synoptic surveys. J Geophys Res 101:16491–16508. https://doi.org/10.1029/96JC01249

Zhang R, Delworth TL (2007) Impact of the atlantic multidecadal oscillation on North Pacific climate variability. Geophys Res Lett 34:229–241. https://doi.org/10.1029/2007GL031601

Zweng MM et al (2013) World ocean Atlas 2013, volume 2: salinity. Levitus S (Ed) A. Mishonov technical Ed.; NOAA Atlas NESDIS 74, 39 pp